

# Active flow control using pulsed micro-jets on a full-scale production car

Jean-Luc AIDER<sup>a</sup>, Pierric JOSEPH<sup>b</sup>, Tony RUIZ<sup>c</sup>, Philippe GILOTTE<sup>d</sup>,  
Yoann EULALIE<sup>d</sup>, Christophe EDOUARD<sup>e</sup>, Xavier AMANDOLESE<sup>f</sup>

<sup>a</sup>Laboratoire PMMH, UMR7636 CNRS, ESPCI ParisTech, 10 rue Vauquelin, 75231 Paris, FRANCE

E-mail: aider@pmmh.espci.fr

<sup>b</sup>Institut Aérotechnique (IAT), 15 rue Marat, 78210 Saint-Cyr-l'Ecole, FRANCE

E-mail: pierric.joseph@cnam.fr

<sup>c</sup>PSA Peugeot Citroën DRIA/DSTF/SFTA, 2 route de Gisy, 78943 Vélizy-Villacoublay Cedex, FRANCE

E-mail: tony.ruiz@mpsa.com

<sup>d</sup>Plastic Omnium Auto Extérieur Services (POAES), Parc Industriel de la Plaine de l'Ain, 01150 Saint-Julie, FRANCE

E-mail: pgilotte@plasticomnium.com, yoann.eulalie@plasticomnium.com

<sup>e</sup>FLOWDIT, 2 rue professeur Paul Milleret, 25000 Besançon, FRANCE

E-mail: christophe.edouard@flowdit.com

<sup>f</sup>Aerodynamics Department, CNAM, 15 rue Marat, 78210 Saint-Cyr-l'Ecole, FRANCE

E-mail: xavier.amandolese@cnam.fr

## Abstract

This paper presents experimental flow control results obtained on a full-scale production car in a wind tunnel. The aim of this paper is to demonstrate the feasibility of controlling the separated flow over the rear part of the car by using pulsed micro-jets. Pulsed micro-jets are produced by hybrid actuators mixing both standard and MEMS (Micro Electro Mechanical Systems) technology. Both actuation frequency and injected momentum are studied. Experiments show a small influence on the drag force (less than 1% reduction), but a stronger one on the lift force (up to 9% reduction). Wall pressure coefficients measurements highlight the suppression of the recirculation bubble over the rear window, along with a reinforcement of the longitudinal C-pillars vortices. Spectral measurements in the shear layer above the rear window show that most efficient control frequencies match the shear layer instability frequency, and that the actuation suppresses the energetical contribution associated with the recirculation bubble frequency. Additional measurements demonstrate that a minimum threshold value of the momentum coefficient is needed for the flow actuation to be efficient. This is the first experimental evidence of the efficiency of micro perturbations (380 $\mu$ m thick micro-nozzles) to control flow separation on a full-scale production car. This is a very important step in the perspective of future applications of flow control in automotive industry to improve aerodynamics performances and reduce CO<sub>2</sub> emissions.

## 1. INTRODUCTION

Nowadays automotive manufacturers are urged to lower the CO<sub>2</sub> emissions and fuel consumption of their vehicles to accommodate with the natural resources rarefaction. Various solutions are now being considered: engine optimization, alternative motorization (electric or hybrid motorization), weight reduction or aerodynamics optimization. For high velocities (higher than 90 km.h<sup>-1</sup>), aerodynamics becomes one of the most interesting levers to minimize the fuel consumption. Since the shapes of the cars are also a compromise with other strong constraints like security, habitability or design, aerodynamics optimization using only shape optimization is limited. One can cite here a recent effort to achieve a compromise between these constraints by Mercedes-Benz with their bio-inspired concept-car Bionic. Inspired by the box-fish shape, the concept-car claimed a very low drag coefficient ( $C_d =$

0.19). Flow control, either passive, active or reactive [1], appears like the only way to reduce aerodynamics forces without altering its design. If its application to the automotive industry seems a really promising way for optimization of cars aerodynamics, there are still many problems to tackle. Actually, flow control may open new possibilities for car designers who could propose badly aerodynamically shaped vehicles, but in those cases the aerodynamicist has to deal with many new constraints: architecture, weight, cost, energy consumption of the actuators used for flow control have to be taken into account in the conception process of the vehicle. As a consequence, the constraints are very strong on the flow control actuators: they should be as small, light, low-cost, low consumption as possible. This is the reason why up to now there has been no industrial application of active flow control on a production vehicle. From this point of view, MEMS (Micro Electro Mechanical Systems) actuators seem to be the realistic choice in the perspective of automotive applications. Unfortunately, if control applied to a 3D bluff-body has been demonstrated, it is still necessary to show that it is possible to control the flow over a real vehicle with micro-perturbations.

Active control of separated flows has been studied for decades by the scientific community, and a lot of successful studies can be found on academic geometry: backward-facing ramp [2], axisymmetric diffuser [3], airfoil [4], blunt plate [5,6] or backward facing step [7,8]. A lot of work is also devoted to a simplified car model, the Ahmed body [9]. Various active technics have been successfully applied: plasma actuators [10], continuous suction [11] or blowing [12] active vortex generators [13] or synthetic jets [14,15]. In a previous study [16], Joseph et al. have successfully applied pulsed jets to the Ahmed body, by reducing its drag coefficient by 8%. They also demonstrated, on the same model [17], that the use of pulsed micro-jets produced by micro-actuators built with MEMS (Micro Electro Mechanical Systems) technology allows to obtain similar drag reduction (up to 12.5%) but with a positive power balance and a greater efficiency than with standard technology, which is the key point for an industrial application.

However, only a few studies can be found in the literature regarding active control of the flow around realistic car shape, like for example the one of Heinemann et al. [18], and even less on full scale, real cars. One can cite here the pioneering work of Aider & Lasserre on the two Citroën concept-cars C-AirLounge (2003) and C-SportLounge (2005) using many flow control systems like active vortex generators, preliminary versions of pulsed micro-jets, an underbody moving spoiler or a system taking air on the front part of the vehicle to create an air curtain around the front wheels, among others. One can also cite the first integration of synthetic jets on the top of the rear slant of the Renault concept-car Altica (2006). Nevertheless, all these innovations were integrated on concept-cars. Only a few could be integrated in a production car. The most recent example is the integration of a system creating an air curtain around the front wheels of the Citroën DS5. Consequently, the aim of this study is to demonstrate that it is possible to control the separated flow over the rear slant of a full size production car with micro-jets produced by micro-actuators matching industrial standards similar to the ones applied when new equipments must be integrated. On a first part, the experimental setup will be described, and some details will be provided about test car, wind tunnel and measurement systems. Next part will describe briefly the base flow in terms of aerodynamics forces and pressure repartitions, but also with the help of oil flow visualizations. Last part will deal with flow control experiments, by focusing on the influence of actuation frequency and injected momentum on both drag forces and wall pressure distribution.

## 2. EXPERIMENTAL SETUP

### 2.1 Test vehicle: Citroën C6

The aim of this study is to evaluate the application of previous findings [16,17] on a generic quarter-scale car model onto a full scale production car. To apply similar control strategies, a car with a similar rear flow had to be chosen. As a reminder, the 25° slant angle Ahmed body previously studied exhibits partial flow separation associated with a pair of strong longitudinal vortices. The rear part of the Citroën C6 seems promising to obtain such features.

The C6 geometric characteristics are depicted on Figure 1. Vehicle length is  $L = 4.908$  m, vehicle width is  $l = 1.860$  m (excluding rear-view mirrors) and vehicle height is  $H = 1.464$  m. In order to avoid ground clearance variation during tests, the hydro pneumatic suspension system is deactivated.

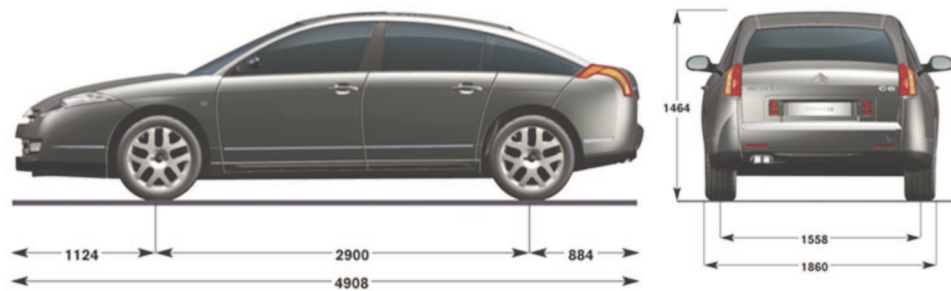


Figure 1. Citroën C6 main dimensions (in millimeters)

Compared to the generic car model, the rear slant geometry appears to be much more complicated (Figure 2). The rear-slant angle is not constant along the span of the rear window, but one can retain its mean value  $\alpha = 35^\circ$  in the symmetry plane of the car. The height  $h$  of the rear slant is  $h = 0.23$  m. In addition, the rear window has a strong concave curvature and is strongly confined by the two C-pillars. It is also important to notice that it is a notchback while the generic car is more a hatchback.



Figure 2. Rear window geometry details with mean slant angle in the symmetry plane

## 2.2 Wind tunnel and measurement systems

Experiments were carried out in the S4 full-scale automotive wind tunnel at the Institut Aérotechnique (IAT, France). This installation provides freestream flow velocities  $U_0$  up to  $44 \text{ m}\cdot\text{s}^{-1}$  with a turbulence ratio of 1.2%. This is a classic external flow condition for wind-tunnel testing. In real world, the external flow can vary in time and can be different from the wind tunnel testing. Using active flow control is also important for this reason: one can vary the amplitude of the perturbation depending on varying external flow conditions.

The rectangular cross-section is 5 m wide, 3 m high and 10 m long (Figure 3). The blockage ratio for the experiments is close to 15% but, thanks to the slotted walls of the wind tunnel, this value is acceptable and no additional blockage correction is needed [19].

In this facility, the maximum boundary layer thickness  $\delta$  is  $65 \times 10^{-3}$  m in the middle of the test section for the flow velocities set during tests. This value can be minimized to  $\delta = 25 \times 10^{-3}$  m by mean of a suction device located under the ground in front of the test section.

During tests several kinds of measurements were carried out. Global flow topology was first investigated using surface oil flow visualizations. Mixture was composed of dodécane, titanium dioxide, oleic acid and silicon oil in various proportions. This mixture is applied with a paintbrush on the rear part of the car to visualize friction lines, leading to qualitative information about main flow topology [20]. Wool yarns were also used punctually to confirm some results.

Aerodynamic forces were measured using a build-in, 6 components, aerodynamic balance. Usual precision is respectively 0.05% in the X direction and 0.1% in the Z direction. Pressure repartition was evaluated using static pressure taps located on the half of the rear part (see Figure 4).

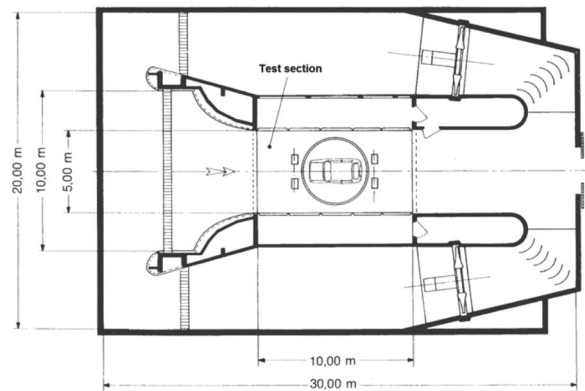


Figure 3. Main dimensions and general arrangement of the IAT-S4 wind tunnel

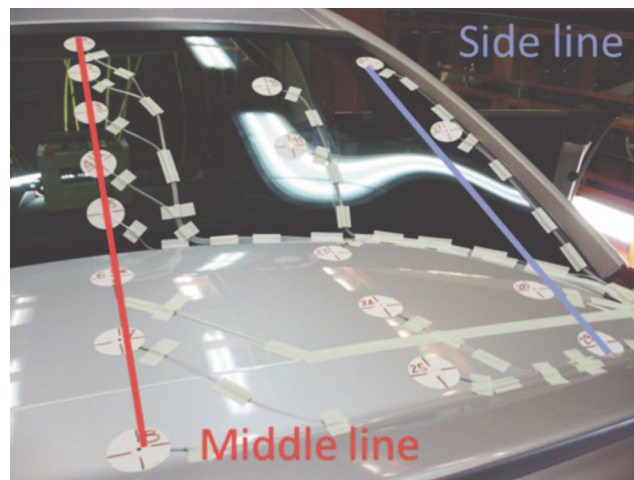


Figure 4. Pressure taps distribution on the rear part of the car

To avoid drillings the walls of the car, external extra-flat sensors were used and connected to a Scanivalve pressure scanner. Measurements precision is usually 0.03% of the full scale with this system. In the present study, a particular attention was given to two lines of pressure taps (called “middle line” and “side line” on Figure 4). In addition, local hot-wire velocity measurements were also carried out in the wake of the car in order to capture first and second velocity moments but also the characteristic frequencies of the wake.

### 3. BASE FLOW

Main characteristics of the base flow around the car were firstly investigated. According to the literature [19] mean base flow behind a notchback geometry is expected to be dominated by a recirculation area enclosed by a strong pair of longitudinal vortices induced by the C-pillars, both on the rear window and the top of the trunk (Figure 5).

#### 3.1 Oil flow and wool yarns visualizations

To investigate the flow topology over the rear part of the model, oil flow visualizations were carried out for a  $U_0 = 30 \text{ m}\cdot\text{s}^{-1}$ , corresponding to a Reynolds number  $Re_L = U_0 L / \nu = 9.8 \times 10^6$  ( $\nu$  being the kinematic viscosity). The rear part of the car was covered with black adhesive in order to obtain good

contrast with the white visualization mixture. Results are presented in Figure 6.

From a global point of view, mean flow topology seems consistent with literature: on the general view (Figure 6a), one can observe the separation area on the rear window associated with a pair of longitudinal vortices on the side (also on Figure 6b). The reattachment point is also present on the trunk, as a singular “saddle point” (also on Figure 6d). The complementary use of wool yarns provides a good estimation of the separation point location on the symmetry line of the rear part of the car (some of them are visible on Figure 2). It appears that the flow doesn't separate exactly at the junction between the roof and the rear slant, but roughly at  $\frac{1}{4}$  LS (LS being the length of the rear slant) from the slant upper edge.

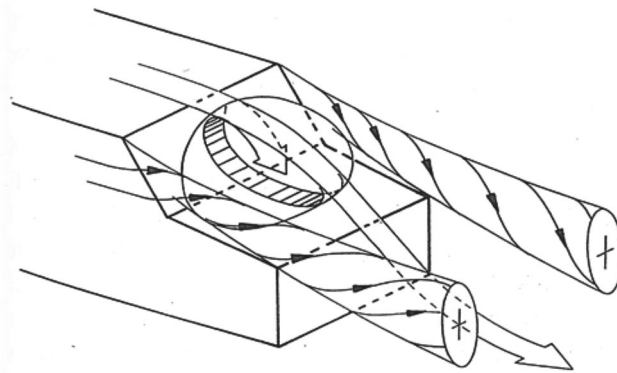


Figure 5. Outline of the mean base flow behind a notchback passenger car [19]

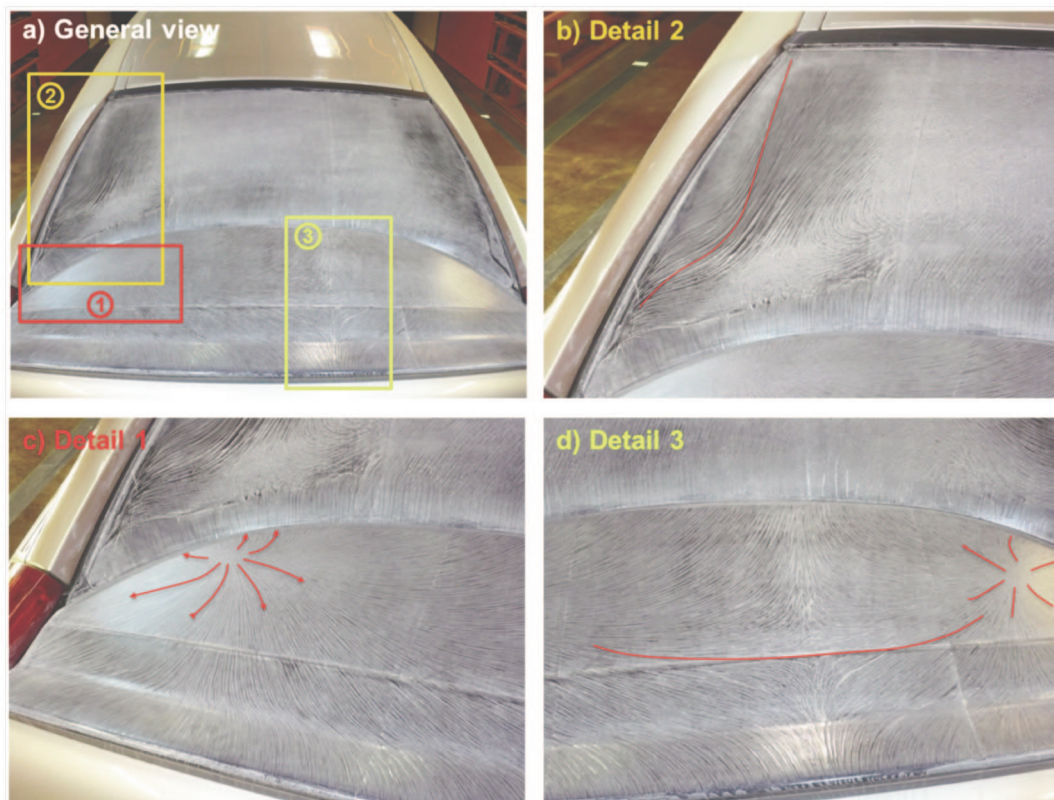


Figure 6. Oil flow visualizations on the rear part of the car: a) general view, b) detail of a longitudinal C-pillar vortex, c) detail of a singular point type focus and d) detail of the reattachment point

In addition, detailed views on Figure 6 indicate some particularities and interesting differences with the classic notchback flow structures. Indeed, the mean topology appears to be more complex than expected: Figure 6c shows singular “foci” points, which indicate the presence of other flow structures. However, this aspect of the flow wasn’t more investigated during the test session.

Another interesting feature is the non-symmetrical aspect of the flow topology. If the longitudinal vortices “prints” seem similar on both sides of the rear window, the central saddle point appears to be switched to the right side of the car (Figure 6d). Reasons for this asymmetry are still under investigation. It may be related to an asymmetry of the vehicle. This is a production car without any simplifications so that its geometry is probably no longer symmetric. However, it is interesting to recall that Lawson et al. [21] found similar results as illustrated on Figure 7.

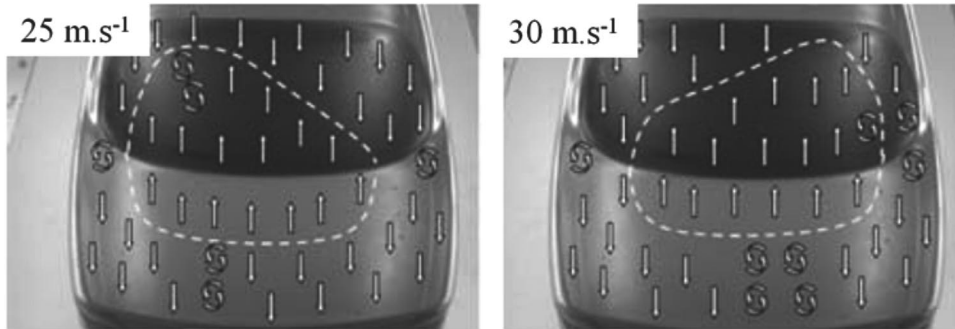


Figure 7. Example of asymmetric flow behind a notchback vehicle [21]

Despite these particularities, mean flow topology is rather close to the expected one, and suitable for flow control experiments.

### 3.2 Drag and lift coefficients

In the following, results of aerodynamic forces measurements without control are presented. Special attention is given to the drag coefficient ( $C_d$ ) and lift coefficient ( $C_l$ ). These coefficients are calculated with the following expressions, with  $F_d$  and  $F_l$  respectively the drag force and lift force and  $S$  the vehicle frontal area.

$$C_d = \frac{F_d}{\frac{1}{2} \rho S U_0^2} \quad (1)$$

$$C_l = \frac{F_l}{\frac{1}{2} \rho S U_0^2} \quad (2)$$

These two coefficients were measured with the aerodynamic balance of the S4 wind tunnel, for several Reynolds numbers:  $Re_L = 8.2 \times 10^6$  ( $U_0 = 25 \text{ m.s}^{-1}$ ),  $Re_L = 9.8 \times 10^6$  ( $U_0 = 30 \text{ m.s}^{-1}$ ) and  $Re_L = 11.4 \times 10^6$  ( $U_0 = 35 \text{ m.s}^{-1}$ ). Results are presented on Figure 8.

First, Figure 8a shows a drag coefficient between 0.328 and 0.329, independent from Reynolds number, with a small 0.3 % increase. These results are close to the manufacturer data obtained in the GIE-S2A wind tunnel:  $C_d = 0.305$ . The 8% difference can be easily explained by taking into account the experimental setup differences: possibly a different ground clearance value and the utilization of moving ground and rotating wheels in the S2A wind tunnel.

On the other hand, on Figure 8b the lift coefficient exhibits a different behavior. One can observe a small decrease (- 2.6 %) of the global lift (green curve) as the Reynolds number increases. Considering the respective contributions on the rear and the front lift coefficients, it appears that the global lift decrease is mainly related to the rear part of the car. Even if this variation is stronger than the one observed on drag coefficient, it is still weak. It is probably related to small modifications of the wake (decrease of the recirculation bubble, stronger C-pillars vortices).

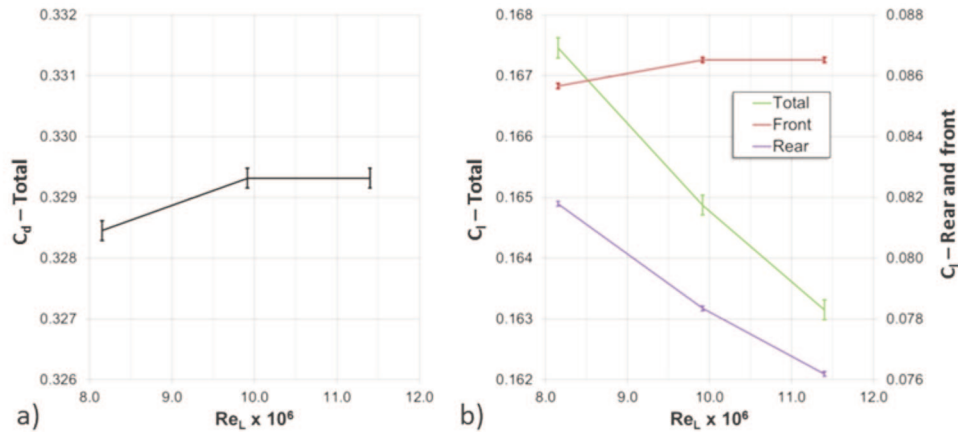


Figure 8. Aerodynamic forces measurements results: a)  $C_d$  and b)  $C_l$  (with rear and front contributions) for various Reynolds numbers

### 3.3 Mean wall-pressure distributions:

Mean wall pressure distribution was measured on various positions on the rear part of the car (see Figure 4). As the pressure taps meshing is relatively low, the analysis is mainly focused on two particular lines: the middle line and the side line (Figure 4). Results are expressed using the pressure coefficient  $C_p$ :

$$C_p = \frac{p - p_0}{\frac{1}{2} \rho U_0^2} \quad (3)$$

with  $p$  the local static pressure at the measurement point and  $p_0$  the undisturbed static pressure. As for the aerodynamic forces, measurements were carried out for various Reynolds numbers ranging between  $Re_L = 6.6 \times 10^6$  ( $20 \text{ m.s}^{-1}$ ) and  $Re_L = 11.4 \times 10^6$  ( $35 \text{ m.s}^{-1}$ ), in order to investigate a possible Reynolds effect. Results are presented on Figure 9 for both pressure taps lines.

The slant area exhibits negatives values of  $C_p$  along both lines, consistent with bluff body wakes. The recirculation bubble starts around pressure tap number 2. There is almost no variation along the middle line up to pressure tap number 7, as expected in a recirculation bubble. On the contrary a small pressure decrease for increasing Reynolds numbers is observed along the side line. It is interesting to notice that this effect is reversed on the top of the trunk for both lines, as the pressure seems to increase with Reynolds number. This effect is particularly strong on the middle line on the pressure tap n°7, which roughly corresponds to the reattachment point. On the rear of the trunk, the wall pressure becomes very small and nearly constant.

This Reynolds effect could be linked to physical mechanisms such as the transition of the boundary layer growing over the roof or / and the modification of the intensity of the longitudinal C-pillar vortices. Both phenomena can influence the position of the separation point and as a consequence the length of the separated region. This can be compared to the transition of separated flows over backward-facing steps or smoothly contoured ramps: the recirculation bubble depends on the Reynolds number and reaches its lowest asymptotic value for larger Reynolds numbers [22,23].

These observations, especially the pressure increase on the pressure n°7, can be also linked to the lift coefficient decrease. On the top of the trunk the pressure is applied on a flat surface parallel to the ground, so a pressure increase on this particular area will have a strong influence on the lift force rather than on the drag coefficient. This is consistent with previous forces measurements.

In fact, the pressure variation is more visible near the reattachment point in the symmetry line. This indicates that this pressure variation is linked to a modification of the central separation bubble, characteristic of this kind of geometry (see Figure 5). As the pressure increases with Reynolds number, it seems that the central area recirculation becomes weaker and so, induces less depression. The pressure decrease observed on the side line (i.e. at the position of the longitudinal vortices) supports

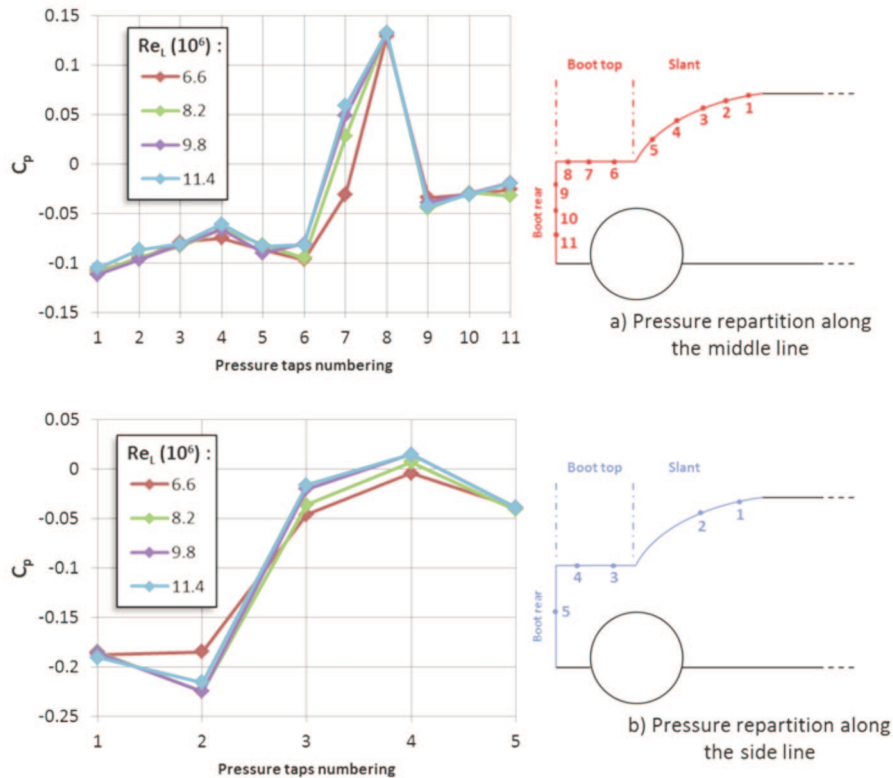


Figure 9. Pressure repartition along a) the symmetry line and b) the side line for various Reynolds numbers

this hypothesis: the C-pillar vortices become stronger and induce an inflow motion which tends to reduce the recirculation bubble. This coupling mechanism between the different flow structures has been observed by various authors like Aider et al. [13], Fourrié et al. [24] or Joseph et al. [16].

The mean flow topology of the car wake is now well described. The following section will deal with flow control experiments. As the characteristics of the flow exhibit some variations with Reynolds number, tests were mainly carried out for only one flow velocity.

#### 4. FLOW CONTROL EXPERIMENTS

As stated in introduction, a lot of relevant control parameters exist within the literature. Some are related to the jets geometry (i.e. size, form and position of the jets), and some others to the jets characteristics (momentum coefficient  $C_{\mu}$ , jet Strouhal number  $St_j$ , time evolution of the jets speed, etc.). In the present study, the jets geometry is fixed by technological constraints, related to both the car and the actuators. The main parameters were thus related to the jets characteristics, especially the actuation frequency, and to a less extent, the momentum coefficient. Before coming to the control results, the control system and the actuators are detailed.

##### 4.1 Description of the control system

The goal of this study is to demonstrate the potential of active flow control from an industrial point of view. This imply to set a cost-effective control action, and to use small, easy to integrate, low-consumption actuators. Such control solution, relying on MEMS actuators, has been described in Joseph et al. [17]. MEMS actuators present both a small size and a good efficiency, but also produce effective control action. One of the major issues is to demonstrate that such micro-perturbations induced by MEMS actuators can still be efficient on a full-scale vehicle.

However, the cost of these actuators is still very high when only a few prototypes are being built. MEMS actuators can become low-cost only when mass production is considered. In the present case, it would have been too expensive to build a full-scale demonstrator using only full silicon MEMS actuators. As a consequence, an hybrid system was designed associating micro-nozzles, built with the same process as the MEMS, with classical magnetic valves (Joseph et al. [16]). This hybrid system,

depicted in Figure 10, is quite affordable and creates the same micro-perturbations as the MEMS actuator on a full-scale car.

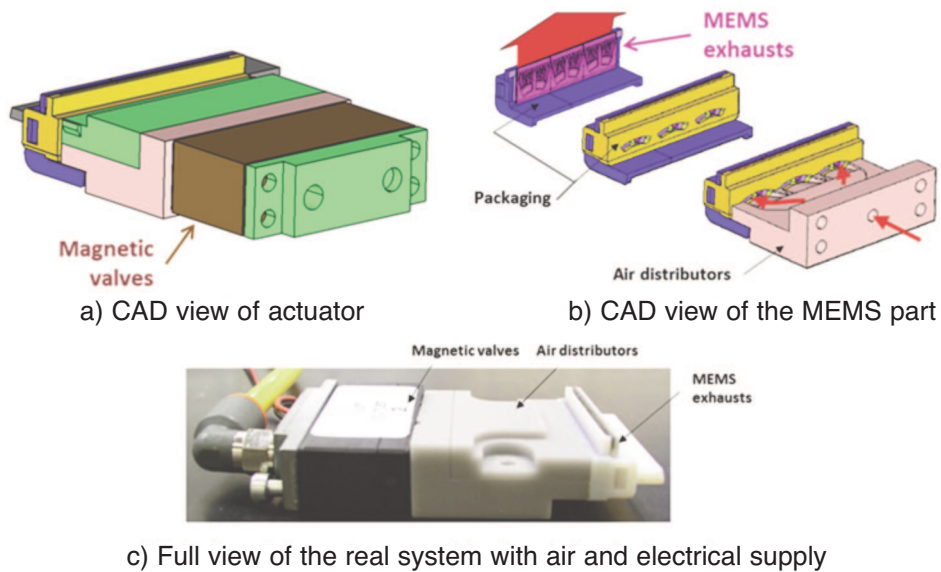


Figure 10. Hybrid actuators: a) full CAD view, b) details of the MEMS part and c) picture of the actuators with air and electrical supply. Each actuator contains three micro-jets.

As shown in Figure 10, the air is pulsed using magnetic valves before coming into a specially designed section which distributes the air flow through three MEMS micro-nozzles, producing three pulsed micro-jets. The distance between the centerlines of two neighboring micro-nozzles is 12 mm. As for the magnetic valves system described in Joseph et al. [16], power supply and frequency generators are needed to drive the jets frequency. The jet speed / injected momentum is set by varying the air supply pressure.

The location of the actuators was chosen in agreement with literature and previous works. Several studies report that controlling the flow immediately at separation point is a very efficient strategy [7,15,16]. However in the present study, technological constraints are very strong since we are dealing with a production car. Flow separation occurs over the rear window, which is a place where actuators can not be integrated. In addition, the goal of this study is to propose a realistic solution from a technological and industrial point of view. The consequence is that there are a very few places into a

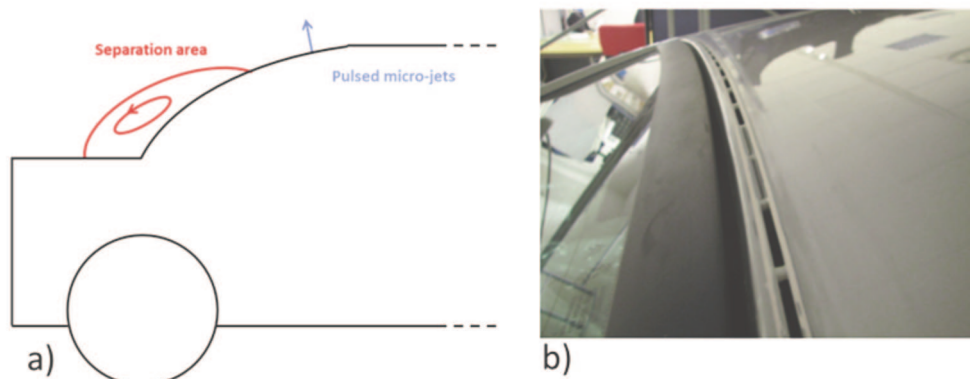


Figure 11. a) Schematic description of the actuation position and the separation area. b) Picture showing the final integration of the actuators at the end of the roof of the C6. Each rectangular slot corresponds to three micro-jets. The pulsed micro-jets are located around 10 cm upstream the separation line.

production car where the actuators can be integrated. The control system was then integrated into an existing spanwise hollow cross-piece at the end of the roof, just upstream the rear window. A schematic description of the actuation location relative of the separation area is shown on Figure 11a.

As depicted on Figure 11b, micro-jets are distributed over the entire width of the rear slant. 21 hybrid actuators (Figure 10) were used. It corresponds to 63 micro-jets (three micro-jets per hybrid actuators). The micro-nozzle's outlet cross-section is rectangular. It is  $0.38 \cdot 10^{-3}$  m thick (along the streamwise direction) and  $2.5 \cdot 10^{-3}$  m long (spanwise direction). The main planar dimensions of of the micro-nozzles are summarized on Figure 12. The micro-jets axis is perpendicular to the wall.

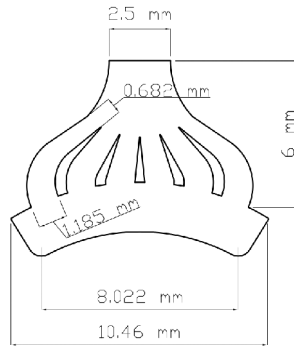


Figure 12. Planar dimensions and geometry of the convergent micro-nozzle which is  $380 \mu\text{m}$  thick.

Taking into account the experimental constraints (a jet frequency  $f_j$  up to 500 Hz, and a flow rate range from  $300 \text{ l}\cdot\text{min}^{-1}$  to  $600 \text{ l}\cdot\text{min}^{-1}$ ), the mean jet velocity  $U_j$  is expected to range between  $87 \text{ m}\cdot\text{s}^{-1}$  to  $174 \text{ m}\cdot\text{s}^{-1}$ . The time evolution of the jet speed is a square signal with a significant overshoot at the beginning of the blowing phase as detailed in Joseph et al. [16]. The duty-cycle is 50%. The jets axis are perpendicular to the wall. The following results were obtained at  $\text{Re}_L = 9.8 \times 10^6$  ( $U_0 = 30 \text{ m}\cdot\text{s}^{-1}$ ).

#### 4.2 Influence of the forcing frequency on aerodynamic forces

The evolution of aerodynamic forces as a function of forcing frequency was investigated using the aerodynamic balance of the S4 wind tunnel. A parametric study was carried out, and the 6 components were measured for various values of adimensional frequency and momentum coefficient. Following results focus on drag and lift coefficients variations. Adimensionnal frequency and momentum coefficient are calculated using the following definitions:

$$C\mu = \frac{\rho S_j U_j^2}{\frac{1}{2} \rho S U_0^2} \quad (4)$$

$$\text{St}_j = \frac{f_j h}{U_0} \quad (5)$$

where  $S_j$  is the outlet cross-section of the jets,  $S$  is the car frontal area and  $h$  the thickness of the jet ( $h = 0.38 \cdot 10^{-3} \text{ m}$ ) and  $h$  is the height of the rear slant. In the following, drag and lift coefficients without control are noted  $C_{d0}$  and  $C_{l0}$ , and  $C_d$  and  $C_l$  with control. Results are expressed as drag and lift coefficients variations (in %) such as  $\Delta C_d = (C_d - C_{d0})/C_{d0}$  and  $\Delta C_l = (C_l - C_{l0})/C_{l0}$ .

First, the influence of the actuation frequency was investigated. The momentum coefficient was fixed to  $C\mu = 0.24$  (corresponding to flow rate of  $600 \text{ l}\cdot\text{min}^{-1}$ ) while the Strouhal number was varied in three different ranges arbitrarily chosen: low frequency range ( $0.05 < \text{St}_j < 0.48$ ), intermediate frequency range ( $1.44 < \text{St}_j < 2.90$ ) and high frequency range ( $2.40 < \text{St}_j < 24.06$ ). Drag coefficient variations are plotted as a function of the Strouhal numbers on Figure 13.

One can observe that influence on drag is weak, as drag variations do not exceed  $\pm 1\%$  (errors are about  $0.05\%$ ). The maximum drag reduction is about  $\Delta C_d = -0.8\%$  for  $\text{St}_j = 1.53$ . It appears that for

the low frequency range ( $0.05 < St_j < 0.48$ ), the drag force is mainly increased by the control action, and that for the intermediate range ( $1.44 < St_j < 2.90$ ) the drag force is rather decreased. However,  $C_d$  gains are not very reliable, as a slight frequency shift cancels the gains.

For the high Strouhal number range, the influence of the Strouhal number is very weak.

The control appears to be less efficient on drag coefficient than the previous results obtained on a simplified model [16,17]. However, it is important to recall here that the present study focus on a real full-scale production car. First, as the car aerodynamics has already been optimized by the car manufacturer, the potential gain is smaller than on the model. In addition, the control strategy focuses on controlling the recirculation bubble on the rear slant of the car. On the model, rear part contribution to the drag is around 70%, depending on the car geometry [9]. For a real, not-simplified, production vehicle the drag coefficient is the result of the contribution of many other sources like underbody flow, wheels and wheel wells, etc. The potential drag reduction by focusing only on the rear part is consequently reduced, especially with a relatively small rear slant as the one of the C6.

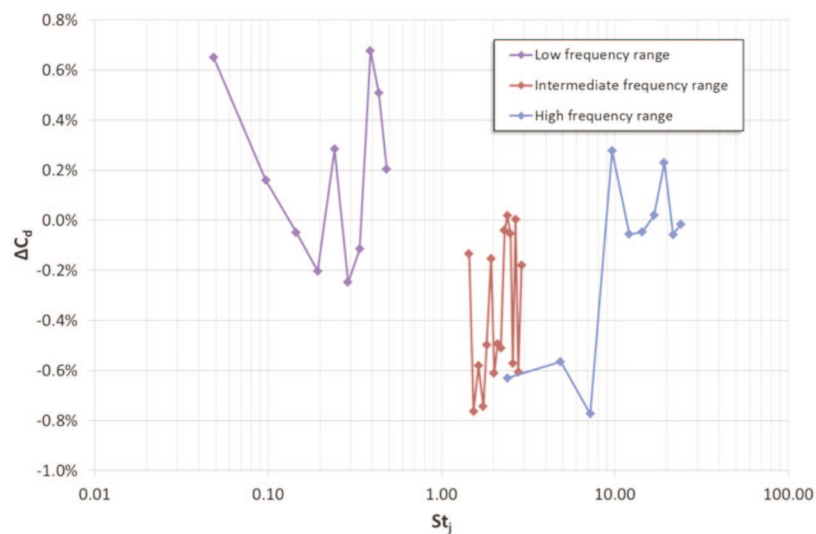


Figure 13. Influence of the Strouhal number on the drag coefficient ( $C_\mu = 0.24$ )

Another important difference is that the vehicle is a notchback so that the contribution of the rear slant flow separation to the overall drag is smaller than for a standard hatchback configuration. The flow control is applied on the upper part of the rear slant which is rather small compared to standard vehicles. The contribution of the rear slant area  $S_{rs}$  to the overall cross-section of the vehicle  $S$  is small ( $S_{rs} / S = 0.13$ ) so that the contribution of the separated flow over the rear slant to the overall drag coefficient is also small. Moreover the Citroën C6 rear slant is original, with a rather small concave rear slant followed by a rather long flat trunk and surrounded by two C-pillars, limiting the interaction between the flow separation and the other large-scale flow structures. For all these reasons, even if the flow separation is cancelled out, the corresponding drag reduction may be small.

On the other hand, a stronger effect on the lift coefficient can be expected if the flow separation is suppressed. Indeed, as shown on Figure 14, the lift coefficient decreases proportionally to the actuation frequency. The best lift reduction is obtained with the highest tested frequency ( $\Delta C_l = -8.6\%$  for  $St_j = 24.06$ ). In addition, it seems that a logarithmic law links both Strouhal number and lift reduction as the lift decrease seems roughly linear on this semi-log scale. By considering  $C_l$  (and not  $\Delta C_l$ ), it appears that the model  $C_l = 0.1747 \times St_j^{-0.024}$  fits well with the experimental measurements.

This result may be surprising, considering the weak effect on the drag coefficient. Nevertheless, one has to recall that a decrease of the lift coefficient has already been highlighted in part 3.1 (Figure 8). Despite that the Reynolds numbers is set during control test, a tentative explanation can be inferred. If the actuation is efficient, then the flow separation is reduced. The lift reduction suggests that the higher the actuation frequency, the larger the reduction of the recirculation bubble over the rear slant. This can be related to the lift reduction as a function of the Reynolds number: the largest the Reynolds number, the smaller the recirculation bubble because of the transition to turbulence of the incoming boundary

layer growing over the roof. Nevertheless, additional tests have to be done to confirm this tentative interpretation. The lift reduction can be interesting in some situations for production cars. Depending on the design, some production cars may lose stability because of a strong lift on the rear axle. This is often the case for notchbacks. The Citroën C6 has precisely a rather large lift, which is the reason why an active spoiler has been integrated at the end of the trunk to improve its stability.

### 4.3 Influence of the forcing frequency on the mean wall-pressure distributions

The previous results obtained on drag coefficients show that it is difficult to understand the real effect of the control through aerodynamic forces measurements. In order to analyze the physical consequences of the control on the flow, much more attention was given in this part to the pressure signature on the rear of the vehicle during the parametric study.

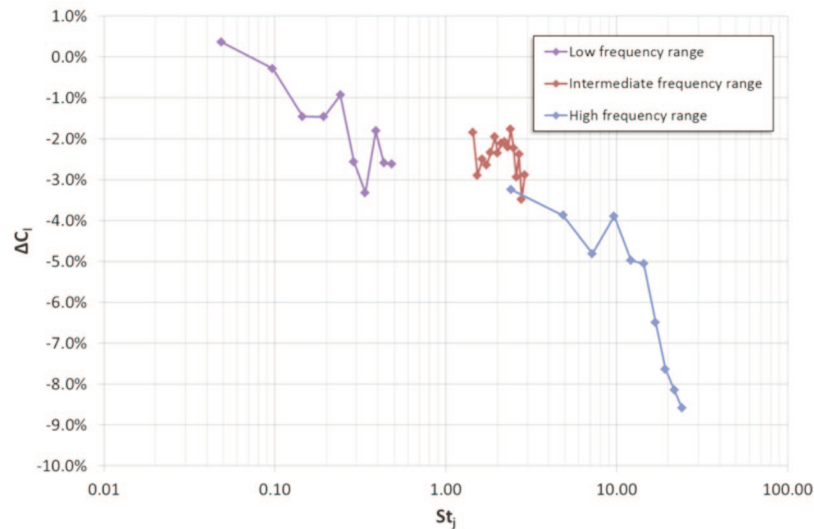


Figure 14. Influence of the Strouhal number on the lift coefficient ( $C_\mu = 0.24$ )

As for the aerodynamic forces measurements, first tests were carried out with a given momentum coefficient ( $C_\mu = 0.24$ ), and for three different Strouhal number ranges: low frequency range ( $0.05 < St_j < 0.48$ ), intermediate frequency range ( $1.44 < St_j < 2.90$ ) and high frequency range ( $2.40 < St_j < 24.06$ ).

Results are analyzed for the three Strouhal number ranges but, as for the drag coefficient variation, it appears that the strongest effect occurs when the actuation frequency varies in the intermediate frequency range ( $1.44 < St_j < 2.90$ ). Pressure coefficient repartitions obtained for this particular range are plotted on Figure 15, along with the reference values.

One can observe that the pressure coefficients distributions is modified on both the slant / rear window and the top of the trunk, where the pressure increases for all the actuation frequencies at almost all measurement locations. This suggests a strong modification of the slant recirculation bubble. This is a confirmation that the micro-jets have indeed a strong effect on the wake of the vehicle, despite a small modification of the drag coefficient. It can also explain the strong modification of the lift coefficient, directly influenced by the pressure distribution over the flat part of the trunk. One can also notice a pressure decrease on the pressure tap N°1 for all Strouhal numbers. This pressure tap is located upstream the separation point (located between pressure taps N°2 and N°3) so that this pressure decrease may be the consequence of the acceleration of the flow caused by the reduction of the separation and injection of momentum into the boundary layer. Similar effects were already reported on a previous study on a simplified car model [16]. On the contrary, no effect can be detected on the rear part of the trunk.

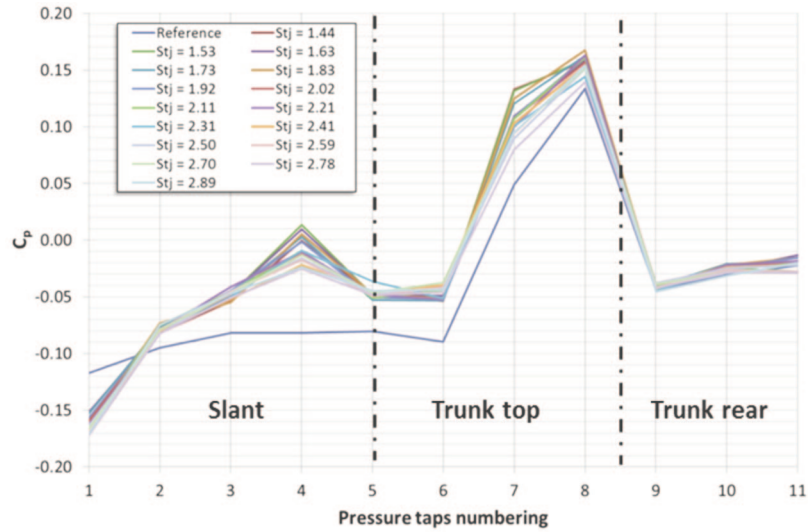


Figure 15. Evolution of the pressure coefficient distribution as a function of the position along the symmetry line of the car for various Strouhal numbers ( $C_{\mu} = 0.24$ ). For the reference flow the separation line is around pressure tap n°2 and reattachment line between pressure taps n°6 and 7.

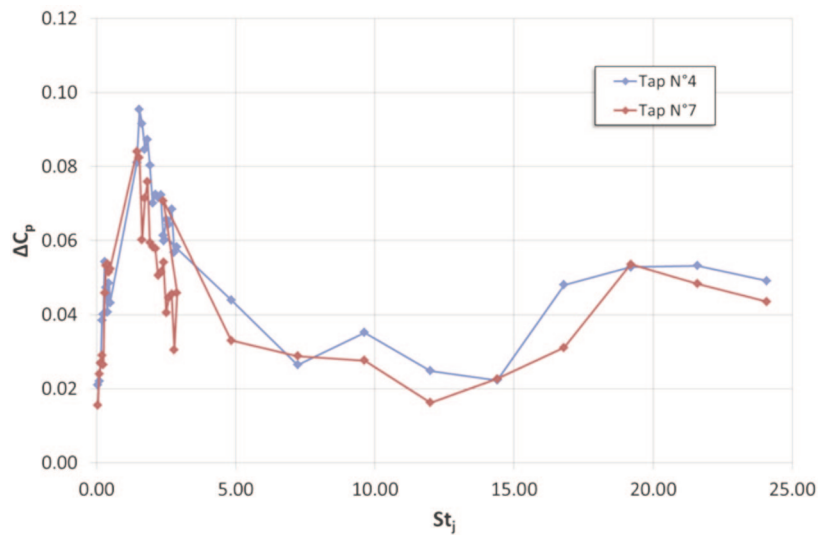


Figure 16.  $C_p$  variations ( $\Delta C_p$ ) on both pressure taps N°4 and N°7 for various Strouhal numbers ( $C_{\mu} = 0.24$ )

In addition, the flow exhibits a strong sensitivity to the actuation frequency for two particular locations: after the separation point (pressure tap N°4 on the Figure 15), and near the reattachment point (pressure tap N°7). Figure 16 shows the pressure recovery  $\Delta C_p = (C_{p0} - C_p)$  as a function of the Strouhal number (for the three studied frequency ranges), with  $C_{p0}$  the reference value and  $C_p$  the controlled value at a given Strouhal number for both the pressure taps N°4 and N°7.

For the best operating point ( $St_j \approx 1.40 - 1.50$ , corresponding to an actuation frequency of 30 - 34 Hz), the pressure recovery is very strong for both locations, and the negative pressure is even canceled in the pressure tap N°4, near the separation point. This most effective frequency is very close to the one which give the better drag reduction ( $St_j \approx 1.53$ ).

Pressure variations measured along the side line (Figure 4 and 9b) are reported on Figure 17. As for the symmetry line, the pressure distribution is strongly modified by the pulsed micro-jets, especially along the slant and the top of the trunk. Results are strongly dependent on the actuation frequency,

which confirms the high sensitivity of the flow in the intermediate Strouhal number range ( $1.44 < St_j < 2.90$ ). However, it appears here that the actuation has a negative effect, especially over the slant region. Pressure coefficient variations for the pressure taps N°2 (on the side of the rear window), and N°3 (on the top of the trunk) are detailed on Figure 18 for the three tested frequency ranges. One can see that on the pressure tap N°2, the pressure coefficient becomes smaller for every actuation frequencies, with a maximum variation of  $\Delta C_p = -0.07$ . On the opposite, the negative pressure on the top of the trunk (pressure tap N°3) is canceled for every tested Strouhal numbers.

In the light of these pressure coefficient variations, it is possible to propose some explanations regarding the weak effect on the drag force. In fact, along the symmetry line of the car, one can notice some pressure increases on both the slant surface and the top of the trunk. Over the rear window, because of its slant, pressure recovery induces a reduction of both the drag and the lift coefficients. Over the top of the trunk, its surface being horizontal, pressure recovery affects only the lift coefficient. Along the side line, the pressure distribution decreases on the slant surface (increasing both drag and lift coefficient), and increase over the top of the trunk (decreasing lift coefficient). As a consequence, one can hypothesize that both effects on drag (increase and decrease) cancel each other, leading to a weak effect on drag. Besides,

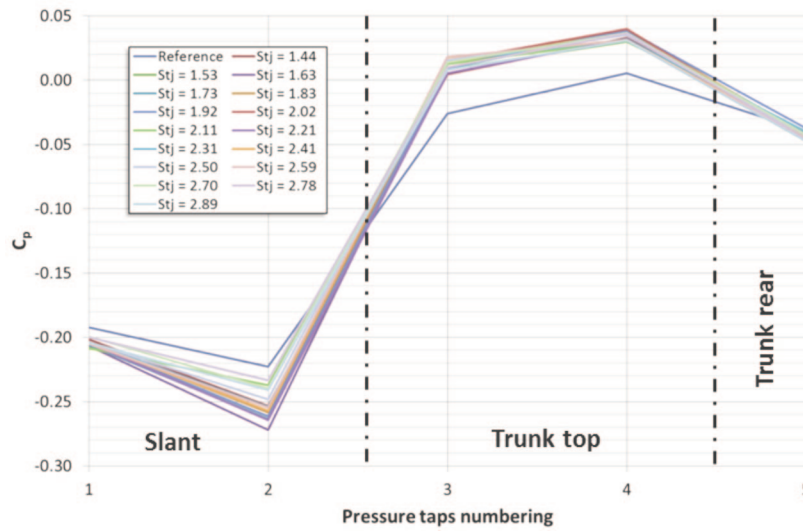


Figure 17. Evolution along the side line of the pressure coefficient distribution as a function of the position along the side of the car for various Strouhal numbers ( $C_\mu = 0.24$ )

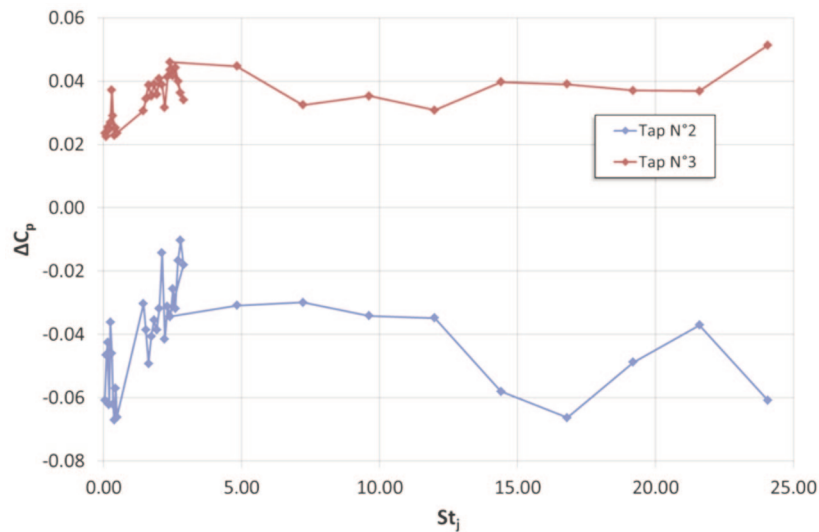


Figure 18.  $C_p$  variations ( $\Delta C_p$ ) on both pressure taps N°2 and N°3 for various Strouhal numbers ( $C_\mu = 0.24$ )

the repeated pressure increase on the top of the trunk is consistent with the observed lift coefficient decrease (but once again, more investigations are needed to state about this particular point).

These pressure variations are also consistent with the chosen control actuation and seem very similar to the conclusion drawn from a previous study on a quarter scale model [16]. In fact, controlling the flow along the separation line mainly affects the recirculation bubble over the rear slant and explains the pressure recovery on the symmetry line. However, as for the classical Ahmed body, a strong interaction exists between the different flow structures of the wake. The weakening of the central recirculation area may lead to a reinforcement of the longitudinal vortices, and to a decrease of the pressure measured on the side line, leading to an increase of the drag.

#### 4.4 Effect of the injected momentum on the mean wall-pressure distributions

This section focuses on the influence of the momentum coefficient. This parameter is very important when considering the energy balance of the control which is critical for applications of flow control to automotive aerodynamics. Several additional tests were carried out by varying the  $C_\mu$ . Several flow rates were tested: from 50 l.min<sup>-1</sup> to 500 l.min<sup>-1</sup>, corresponding to  $C_\mu = 0.002$  and  $C_\mu = 0.16$ . Figure 19 presents the pressure coefficient repartition along the middle line for these different  $C_\mu$  values at a fixed Strouhal number ( $St_j \approx 1.53$ ).

Figure 19 exhibits a very similar pattern to Figure 15. The flow presents high sensitivity to the control parameters, especially near the separation point (pressure tap N°4) and the reattachment point (pressure tap N°7). On the pressure tap N°4, one can see that the pressure recovery increases proportionally to the injected momentum. It also appears that the lowest tested value ( $C_\mu = 0.007$ ) deteriorates the control performance by decreasing the pressure.

Before concluding on the relative importance of both tested parameters (actuation frequency, and injected momentum), it is important to notice that results on Figure 19 were obtained for  $St_j = 1.53$ . As stated before, this frequency is the one offering the best results, both in drag coefficient reduction and pressure increase over the rear part of the car. Tests were also carried out by varying the injected momentum for a different frequency ( $St_j = 7.2$ ). Figure 20 presents the coefficient pressure variation ( $\Delta C_p$ ) on the pressure tap N°4 for both actuation frequencies.

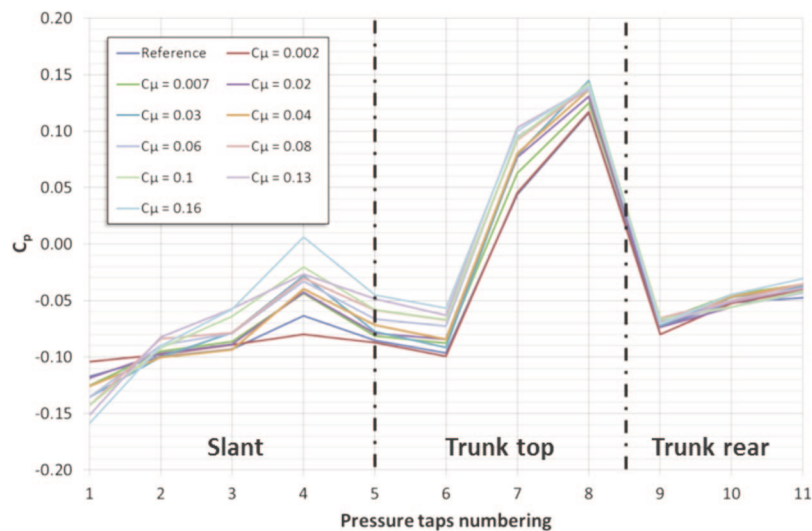


Figure 19. Evolution of the pressure coefficient as a function of the position along the symmetry line on the rear part of the car for various flow rates ( $St_j = 1.53$ ). For the reference flow the separation line is around pressure tap n°2 and reattachment line between pressure taps n°6 and 7.

On Figure 20, one can observe that even if the pressure recovery is similar for both frequencies at lower  $C_\mu$ , the control action becomes more efficient at higher  $C_\mu$  with the appropriate frequency. This is interesting, because it demonstrates that both parameters play an important role in obtaining efficient control results. To be efficient, the flow actuations has to act on a well defined frequency band probably

corresponding to a given flow mechanism. Moreover one can see that there is a critical minimum momentum injection needed for pulsed actuation to play a role. When this threshold is reached ( $C\mu = 0.5$ ), one can see that pulsing at a lower frequency ( $St_j = 1.53$ ) is more efficient. Below this threshold, the perturbation is quickly dissipated because of its too low energy.

In the perspective of drag reduction of a given vehicle, the choice of the injected momentum seems very simple: the best one is the lowest one allowing a positive power balance between the power used for actuation and the power gained through drag reduction. On the contrary, the choice of the actuation frequency seems more subtle and relies on a good knowledge of the spectral content associated with the wake of the car. In the following section, some PSD (Power Spectral Density) measurements realized behind the vehicle are presented, in order to clarify the choice of the actuation frequency.

#### 4.5 Unsteady velocity measurements with and without control in the wake of the car

Several measurements were carried out in the shear layer along a vertical line starting at the bottom of the rear window without control (Figure 21). For each measurement points, mean flow velocity and local turbulence were measured using a single component hot wire probe and a motorized explorer. For each measurements points, the velocity was recorded and averaged over 60 s with a 4000 Hz sample frequency, for  $Re_L = 8.2 \times 10^6$  ( $U_0 = 25 \text{ m}\cdot\text{s}^{-1}$ ).

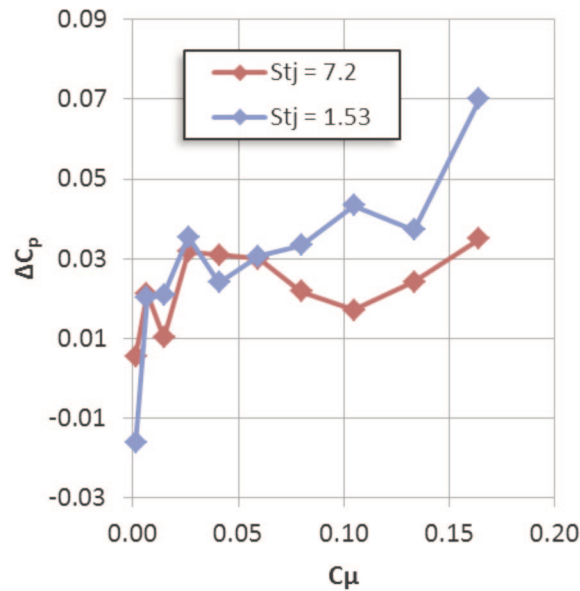


Figure 20.  $C_p$  variations ( $\Delta C_p$ ) on pressure tap N°4 for  $St_j = 1.53$  and  $St_j = 7.2$

Figure 22 also presents power spectral densities for each measurement points for the uncontrolled case. Natural frequencies measurements in the flow are expressed as a Strouhal number  $St$ :

$$St = \frac{fh}{U_0} \quad (6)$$

Mean velocity measurements above the rear part of the car (Figure 21) present a classical shear layer profile, with a strong mean velocity variation between the external free flow ( $Z > 0.25 \text{ m}$ ) and the wake area. The vertical profile of the velocity fluctuations exhibits a maximum at  $Z = 0.2 \text{ m}$  which corresponds to the middle of the shear layer. On Figure 22, this particular point exhibits a very interesting spectral content. One can notice two phenomena emerging from the spectrum for  $St \approx 0.2 - 0.3$  and  $St \approx 2.1$ . This organization, with a low frequency phenomenon and a high frequency one, is very similar to the one observed on the small scale model used in a previous study [16]. As a reminder, the low frequency organization was identified as a global instability of the recirculation area, while the high frequency was related to the shear layer instability.

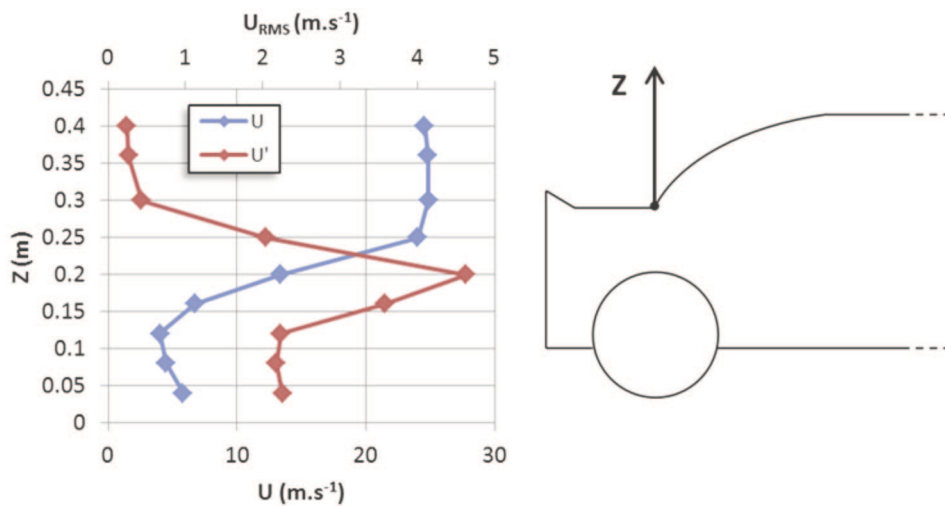


Figure 21. Hot wire measurement in the shear layer without control (mean velocity  $U$  and fluctuations  $U'$ )

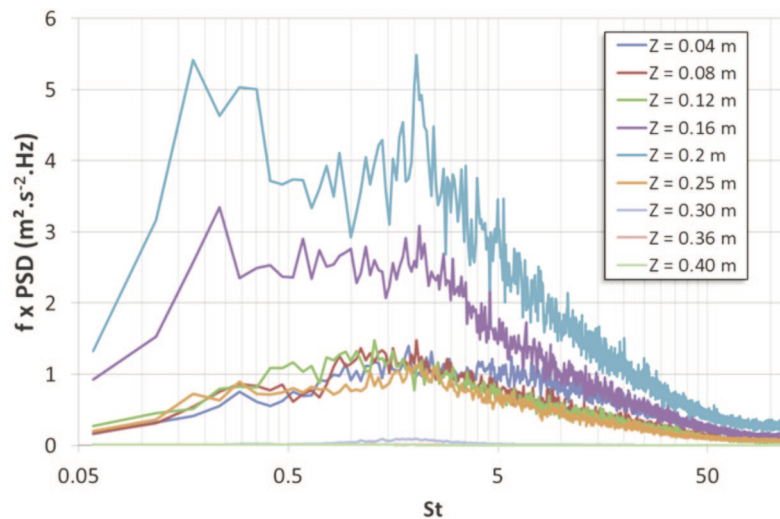


Figure 22. Power spectral densities associated with hot wire measurements (without control)

Figure 23 plots power spectral density with and without control at the point  $Z = 0.2$  m. Injected momentum is set to the maximum ( $C\mu = 0.24$ ) and the actuation frequency to  $St_j = 2.91$  (note that even this frequency is not the optimal one, it is still close to the most effective intermediate frequency range). First, one can notice that the so called “intermediate range” of actuation frequency ( $1.73 < St_j < 3.48$  for  $U_0 = 25 \text{ m.s}^{-1}$ ) roughly corresponds to the large bump associated with the high frequency phenomenon at  $St_i \approx 2.1$ , and that the actuation frequency at  $St_i = 2.91$  is very well defined on the controlled (red) spectrum. Secondly, it appears that the actuation induces a strong decrease of the low frequency organization ( $St_i \approx 0.2 - 0.3$ ). This is consistent with a reduction of the recirculation area, as this phenomenon seems linked to this particular flow structure. To summarize, the recirculation bubble is suppressed over the rear slant (the low frequency signature no longer exists) by the actuation. The frequency measured in the shear layer is no longer the natural shear layer frequency but the one imposed by the pulsed micro-jets.

It appears that the control mechanisms are very similar between the full scale car and the reduced scale model previously studied, and this despite the huge scale and geometry differences. In both cases,

it seems that setting an excitation frequency in the range of the shear layer instability allows for the reduction of the recirculation bubble over the slanted surface.

## 5. CONCLUSION

In the present study, active flow control by pulsed micro-jets has been applied to a full size production car. Base flow has been first investigated and both flow topology and aerodynamic forces appear to be consistent with literature on reduced scale model. Mean wall-pressure distributions show a weak Reynolds effect with, as a consequence, a slight decrease of the lift force as the Reynolds number increases.

Active flow control has been realized using micro-jets produced by hybrid actuators combining MEMS technology for micro-nozzles design and fabrication with classical magnetic valves for pulsed actuation. Blowing is realized immediately upstream the top of the rear glass at the roof end. This location is a compromise between the most efficient location found in a previous study on a reduced scale model, and a realistic implantation on the car regarding industrial constraints. The strategy applied here is to modify the incoming boundary layer and developing shear layer in order to act on the slant recirculation bubble.

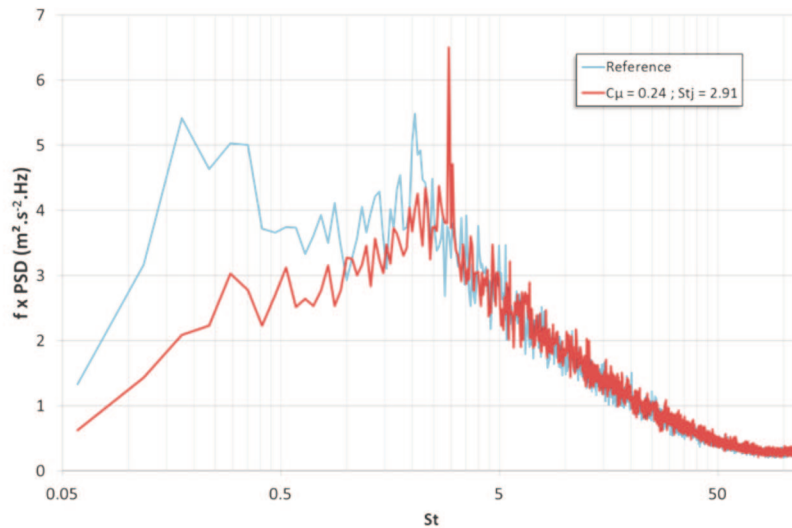


Figure 23. Power spectral densities measured at the  $Z = 0.2$  m position without control, and with control with  $C_{\mu} = 0.24$  and  $St_j = 2.91$

A parametric study has been carried out varying both the actuation frequency and the injected momentum. Both aerodynamic forces and mean wall-pressure distributions have been monitored during control tests. Effects on global drag force are less than 1% reduction. The lift force is decreased up to 9%, even though more investigations are needed regarding this last result. On the other hand, physical flow characteristics have been extracted from the wall pressure signature. It appears that the applied flow control strategy acts favorably on the targeted flow structure, by increasing the pressure over the symmetry plane of the car. In the same time, pressure is reduced under the longitudinal vortices induced by the C-pillars on the side of the rear window due to a coupling mechanism with the recirculation bubble. It seems that the increase pressure loss induced by the longitudinal vortices together with the relatively small surface of the rear slant explain the weak drag reduction.

Spectral analysis of velocity fluctuations in the shear layer reveals a low and high frequency, corresponding respectively to recirculation bubble instability and shear layer instability. In the present case, it seems that the most efficient control frequency match the shear layer frequency. When the control is applied, the energetic contribution associated with the recirculation bubble frequency nearly vanishes and only the actuation frequency can be recovered in the shear layer spectrum, which is consistent with the applied control strategy.

This study demonstrates the feasibility of active control of the separated flow over the rear part of a full size automotive vehicle. Despite the weak effect on drag, those results prove that it is possible to

prevent flow separation over the rear slant of a real full-scale vehicle using micro- perturbations induced by pulsed micro-jets. It demonstrates that a typical automotive wake can be modified using micro-jets that could be produced by small MEMS actuators, easy to integrate in a real production car. The next steps are now to use real MEMS micro-actuators on a full-scale vehicle with a classic hatchback geometry. It would be also important to search for more efficient control strategies taking into account the coupling mechanisms between the different structures composing the 3D wake.

## ACKNOWLEDGEMENTS

This work was carried out in the framework of the CARAVAJE project supported by the Agence pour le Développement Et la Maîtrise de l'Énergie (ADEME). We thank the Renault SA and PSA Peugeot-Citroën Aerodynamics Research teams and the Plastic Omnium research team for fruitful discussions. Technical support by the S4 Wind Tunnel team is also gratefully acknowledged. N. Gautier (Laboratoire PMMH – CNRS) is also gratefully acknowledged for his help in some of the wind tunnel measurements. Many thanks to Flowdit SAS for support concerning MEMS actuators.

## REFERENCES

- [1] Gad-el-Hak, M., *Flow Control: Passive, Active, and Reactive Flow Management*, Cambridge University Press, Cambridge, 2000.
- [2] McManus, K.R., Legner, H.H. and Davis, S.J., Pulsed Vortex Generator Jets for Active Control of Flow Separation, in: *25th AIAA Fluid Dynamics Conference*, Colorado Spring, 1994, 1–12.
- [3] Brunn, A. and Nitsche, W., Separation control by periodic excitation in a turbulent axisymmetric diffuser flow, *Journal of Turbulence*, 2003, 4, 1–13.
- [4] McCormick, D.C., Boundary Layer Separation Control with direct Synthetic jets, in: *Proceedings of 38th Aerospace Sciences Meeting and Exhibit*, Reno, 2000, 1–11.
- [5] Pastoor, M., Henning, L., Noack, B.R., King, R. and Tadmor, G., Feedback shear layer control for bluff body drag reduction, *Journal of Fluid Mechanics*, 2008, 608, 161–196.
- [6] Krajnović, S. and Fernandes, J., Numerical simulation of the flow around a simplified vehicle model with active flow control, *International Journal of Heat and Fluid Flow*, 2011, 32, 192–200.
- [7] Chun, K.B. and Sung, H.J., Control of turbulent separated flow over a backward-facing step by local forcing, *Experiments in Fluids*, 1996, 21, 417–426.
- [8] Duriez, T., Aider, J.-L., Wesfreid, J.-E. and Artana, G., Control of a massively separated flow through vortex pairing and phase locking, submitted to *European. Journal of Mechanics - B/Fluids*, available on arXiv preprint arXiv:1405.4234, 2014.
- [9] Ahmed, S., Ramm, G. and Faltin, G., Some Salient Features of the Time-Averaged Ground Vehicle Wake, *SAE 840300*, 1984, 1–31.
- [10] Boucinha, V., Weber, R. and Kourta, A., Drag reduction of a 3D bluff body using plasma actuators, *International Journal of Aerodynamics*, 2011, 1, 262–281.
- [11] Rouméas, M., Gilliéron, P. and Kourta, A., Drag reduction by flow separation control on a car after body, *International Journal for Numerical Methods in Fluids*, 2008, 60, 1222–1240.
- [12] Krajnović, S. and Basara, B., LES of the Flow around Ahmed Body with Active Flow Control, *Turbulence and Interactions*, 2010, 110, 247–254.
- [13] Aider, J.-L., Beaudoin, J.-F. and Wesfreid, J.-E., Drag and lift reduction of a 3D bluff-body using active vortex generators, *Experiments in Fluids*, 2009, 48, 771–789.
- [14] Krajnović, S., Östh, J. and Basara, B., LES study of breakdown control of A-pillar vortex, *International Journal of Flow Control*, 2010, 2, 237–258.
- [15] Kourta, A. and Leclerc, C., Characterization of synthetic jet actuation with application to Ahmed body wake, *Sensors and Actuators A: Physical*, 2013, 192, 13–26.
- [16] Joseph, P., Amandolèse, X. and Aider, J.-L., Drag reduction on the 25° slant angle Ahmed reference body using pulsed jets, *Experiments in Fluids*, 2012, 52, 1169–1185.
- [17] Joseph, P., Amandolese, X., Edouard, C. and Aider, J.-L., Flow control using MEMS pulsed micro-jets on the Ahmed body, *Experiments in Fluids*, 2013, 54, 1–12.

- [18] Heinemann, T., Springer, M., Lienhart, H., Kniesburges, S. and Becker, S., Active Flow Control on a 1:4 Car Model, in: *16th International Symposium on Applications of Laser Techniques to Fluid Mechanics*, Lisbon, 2012, 1–11.
- [19] Hucho, W.H., *Aerodynamics of Road Vehicles: From Fluid Mechanics to Vehicle Engineering*, 4th edn., SAE, Warrendale, 1998.
- [20] Gilliéron, P., La technique des visualisations pariétales, *Aérodynamique Appliquée*, 2000, 19–26.
- [21] Lawson, N.J., Garry, K.P. and Faucompret, N., An investigation of the flow characteristics in the bootdeck region of a scale model notchback saloon vehicle, in: Garner, C., ed., *Proceedings of the Institution of Mechanical Engineers, Part D: Journal of Automobile Engineering, Loughborough, 2007*, 221, 739–754.
- [22] Armaly, B.F., Durst, F., Pereira, J.C.F., and Schönung, B., Experimental and theoretical investigation of backward-facing step flow, *Journal of Fluid Mechanics*, 1983, 127, 473–496.
- [23] Gautier, N. and Aider, J-L. 2013a Control of the separated ow downstream a backward-facing step using real-time visual feedback. *Royal Society Proceedings A.*, 2013, 469, 20130404.
- [24] Fourrié, G., Keirsbulck, L., Labraga, L. and Gilliéron, P., Bluff-body drag reduction using a deflector, *Experiments in Fluids*, 2011, 50, 385–395. and Gilliéron, P.,